

# A Magnetically Guided Self-Rolled Microrobot for Targeted Drug Delivery, Real-Time X-Ray Imaging, and Microrobot Retrieval

Kim Tien Nguyen, Gwangjun Go, Zhen Jin, Bobby Aditya Darmawan, Ami Yoo, Seokjae Kim, Minghui Nan, Sang Bong Lee, Byungjeon Kang, Chang-Sei Kim, Hao Li,\* Doyeon Bang,\* Jong-Oh Park,\* and Eunpyo Choi\*

Targeted drug delivery using a microrobot is a promising technique capable of overcoming the limitations of conventional chemotherapy that relies on body circulation. However, most studies of microrobots used for drug delivery have only demonstrated simple mobility rather than precise targeting methods and prove the possibility of biodegradation of implanted microrobots after drug delivery. In this study, magnetically guided self-rolled microrobot that enables autonomous navigation-based targeted drug delivery, real-time X-ray imaging, and microrobot retrieval is proposed. The microrobot, composed of a self-rolled body that is printed using focused light and a surface with magnetic nanoparticles attached, demonstrates the loading of doxorubicin and an X-ray contrast agent for cancer therapy and X-ray imaging. The microrobot is precisely mobilized to the lesion site through automated targeting using magnetic field control of an electromagnetic actuation system under real-time X-ray imaging. The photothermal effect using near-infrared light reveals rapid drug release of the microrobot located at the lesion site. After drug delivery, the microrobot is recovered without potential toxicity by implantation or degradation using a magnetic-field-switchable coiled catheter. This microrobotic approach using automated control method of the therapeutic agents-loaded microrobot has potential use in precise localized drug delivery systems.

## 1. Introduction

Over the past decades, a variety of targeted therapies have been developed for effective treatment of cancer.<sup>[1–3]</sup> Compared with conventional chemotherapy, targeted therapy can minimize side effects by increasing local concentrations of therapeutic agents such as drugs, messenger RNA (mRNA), genes, radioactive seeds, imaging contrast agents, and proteins at specific target sites in the body while maintaining a lower level of concentrations in the rest of the body.<sup>[4]</sup> More recently, microrobots capable of carrying and delivering therapeutic agents have attracted great interest in cancer treatment.<sup>[5,6]</sup> These microrobots can stably carry therapeutic agents used for targeted therapy and release them in precise and controlled amounts to specific target locations. Furthermore, magnetic fields, ultrasound, and light used as actuation sources for microrobots enable minimal and noninvasive surgery through wireless locomotion of microrobots and can be used as trigger devices that can selectively release drugs.<sup>[7–12]</sup> Therefore, compared to conventional targeted therapy,

Dr. K. T. Nguyen, Dr. G. Go, B. A. Darmawan, A. Yoo, S. Kim, M. Nan, S. B. Lee, Prof. B. Kang, Prof. C.-S. Kim, Prof. D. Bang, Prof. J.-O. Park, Prof. E. Choi  
Korea Institute of Medical Microrobotics  
43-26, Cheomdangwagi-ro 208-beon-gil, Buk-gu, Gwangju 61011, South Korea  
E-mail: doyeonbang@kimiro.re.kr; jop@kimiro.re.kr; eunpyochoi@jnu.ac.kr

Dr. K. T. Nguyen, Dr. G. Go, B. A. Darmawan, M. Nan, Prof. C.-S. Kim, Prof. J.-O. Park, Prof. E. Choi  
School of Mechanical Engineering  
Chonnam National University  
77 Yongbong-ro, Buk-gu Gwangju 61186, South Korea

Prof. Z. Jin  
School of Biomedical Engineering  
Xinxiang Medical University  
Xinxiang Henan 453003, China

Prof. B. Kang, Prof. D. Bang  
College of AI convergence  
Chonnam National University  
77 Yongbong-ro, Buk-gu Gwangju 61186, South Korea

Prof. H. Li  
Department of Mechanical Engineering  
Yanbian University  
Yanji 133002 China  
E-mail: yustlh@ybu.edu.cn

 The ORCID identification number(s) for the author(s) of this article can be found under <https://doi.org/10.1002/adhm.202001681>

DOI: 10.1002/adhm.202001681

microrobots can eliminate the potential side effects caused by circulation of therapeutic agents and selectively deliver more therapeutic agents.<sup>[13,14]</sup> In addition, microrobots can deliver a greater amount of material to provide faster and better recovery. The current trend in microrobot research has focused on delivering therapeutic agents to lesion sites and microrobot degradation inside the body. Therefore, most studies have evaluated the mobility of microrobots and verified the biocompatibility, biodegradability, and drug delivery of microrobots from the perspective of biological effects.<sup>[15–21]</sup> However, current microrobots have limitations in being applied to *in vivo* experiments that require thorough consideration of the procedure, including the conditions before and after the injection and delivery of the microrobot.

In terms of biostability, a microrobot injected into the body must not induce side effects such as exothermic, inflammatory, and immune reactions; should not pose a hazard to cells; and should be nontoxic and noncarcinogenic.<sup>[5,6]</sup> To ensure stability inside the body, microrobots composed of biocompatible and biodegradable materials have been developed using various micro- and nanofabrication methods such as 3D printing,<sup>[15–19]</sup> emulsion layering,<sup>[20]</sup> and electrodeposition.<sup>[21]</sup> Although microrobots have demonstrated nontoxicity in specific cells and biodegradability in specific environments, the potential effects of microrobots and their degraded products locally concentrated on the target site have not been verified. In particular, magnetic nanoparticles (MNPs) carried on a microrobot body for its magnetic actuation can cause significant toxic effects, such as inflammation, the formation of apoptotic bodies, impaired mitochondrial function, membrane leakage of lactate dehydrogenase generation of reactive oxygen species, and chromosome condensation.<sup>[22,23]</sup> In addition, unlike general nanoparticle-based drug delivery circulating in the body through intravenous injection, MNPs released by microrobots concentrated in the lesion may cause more lethal toxicity to normal tissues around the disease because of the high concentrations.<sup>[22]</sup> As an alternative to leaving microrobots in the body, retrievable microrobots can be introduced into drug delivery. The retrievable microrobot can be removed from the body after completing the drug release task to the target site. Therefore, the recoverable microrobot can minimize toxicity-related issues caused by the degradation of the microrobot.

For the targeted drug delivery (DD) task, the robot structure is also considered as an important factor, in which the self-rolling/-folding microrobots are the preferable structures for DD with capable of pick and place and carrying a larger amount of drug/cell.<sup>[24–28]</sup> However, the challenge for applying these type of robots to the *in vivo* experiment is remain opened since it requires to change the environmental temperature to unfold these type of structure and release the drug. On the other hand, the unrolling/unfolding microrobots with the porous cylindrical/helical/spherical structure shows a higher possibility in a practical viewpoint.<sup>[29–34]</sup> The drug/cell is strongly bonded in the porous structures of the robot and gradually release after reaching the target site thanks to its biodegradability<sup>[29–32]</sup> or external stimulus such as Near-infrared (NIR),<sup>[24]</sup> ultrasound,<sup>[33]</sup> or alternative magnetic field (AMF).<sup>[34]</sup>

In addition to the biological structure of microrobots, magnetic targeting is an important aspect for drug delivery using microrobots, making magnetic microrobots superior to for con-

ventional cancer therapy techniques in terms of achieving a successful accessing rate, lowering the risk of infection, and reducing trauma.<sup>[35–38]</sup> Because of their minimal size, magnetic microrobots can reach closer to the target lesions than wire-type surgical tools. There is a need to develop an autonomous microrobot system that can quickly and precisely deliver drugs to lesions based on pathway information, current position, and target point as well as environmental conditions. For real-time imaging techniques of the microrobot, the difficulty of tracking the microrobot through the living organisms remains one of the major challenges in practical viewpoint where the developed 2D-/3D-optical microscope imaging techniques are no longer applicable because of the low penetrating capacity of light through the biological tissue. The photoacoustic imaging technique provides a possibility of *in vivo* tracking of microrobots since it shows a deep penetration into living tissues (up to 2 cm<sup>[33,39]</sup>). The positron emission tomography incorporated with computed tomography (PET-CT) is another promising technique *in vivo* with high resolution.<sup>[40]</sup> However, high initial cost and operating cost are disadvantages from widely applicable in lab-scale research. Recently, X-Ray irradiation is also used to track the metal-coated microparticles/microrobots.<sup>[41]</sup> In addition, most proposed drug delivery systems using magnetic microrobots just take into account how to approach the target areas and trigger the drug release; few of those efforts address the issue of the microrobot remaining inside the tissue or vessel after treatment.<sup>[42–44]</sup> Despite the fact that microrobots used for biomedical application are made of biocompatible and biodegradable materials, they can cause a potential life-threatening condition (e.g., vessel embolism) if they are left inside the human body.<sup>[45]</sup> To deal with post complications of microrobot remaining inside the target site after functioning, some efforts demonstrated the microrobot retrieval trials.<sup>[34,46]</sup> Unfortunately, the completed procedure for *in vivo* application remains opened in which only a simple *in vitro* retrieval of microrobots under magnetic guidance is implemented.<sup>[34]</sup> A remarkable idea of using a magnetic catheter includes 27 permanent magnets integrated with a 12Fr catheter to retrieve of nanoagents from the bloodstream.<sup>[46]</sup> This method can passively collect the unused agents which are not accumulated into the tumor. Until now, several studies have been about the drug-carrying micro/nanorobot system, but a microrobot system integrating the fabrication, delivery, and collection functions of the drug-carrying micro/nanorobot into one has not yet been reported.

Therefore, to resolve these issues, we have developed a magnetically guided self-rolled microrobot for autonomous-navigation-based targeted drug delivery, real-time X-ray imaging, and microrobot retrieval, as shown in **Figure 1**. The microrobot consists of a ceramic-based self-rolled body and an MNP-coated surface layer. The ceramic-based composite material used can withstand the fluid environment and is robust during injection and retrieval. Here, E-dent 400 is a ceramic-based composite material, used to form a microrobot body, and is a biocompatible Class IIa and US Food and Drug Administration (FDA)-approved solution for accurate 3D printing of crowns and bridges in dental applications.<sup>[47]</sup> The microrobot body was prepared by a single-layer-based self-rolling technique using focused Ultraviolet (UV) light polymerization. According to this technique, a single-layered material is encoded with an anisotropic density gradient along the longitudinal direction via focused light with a

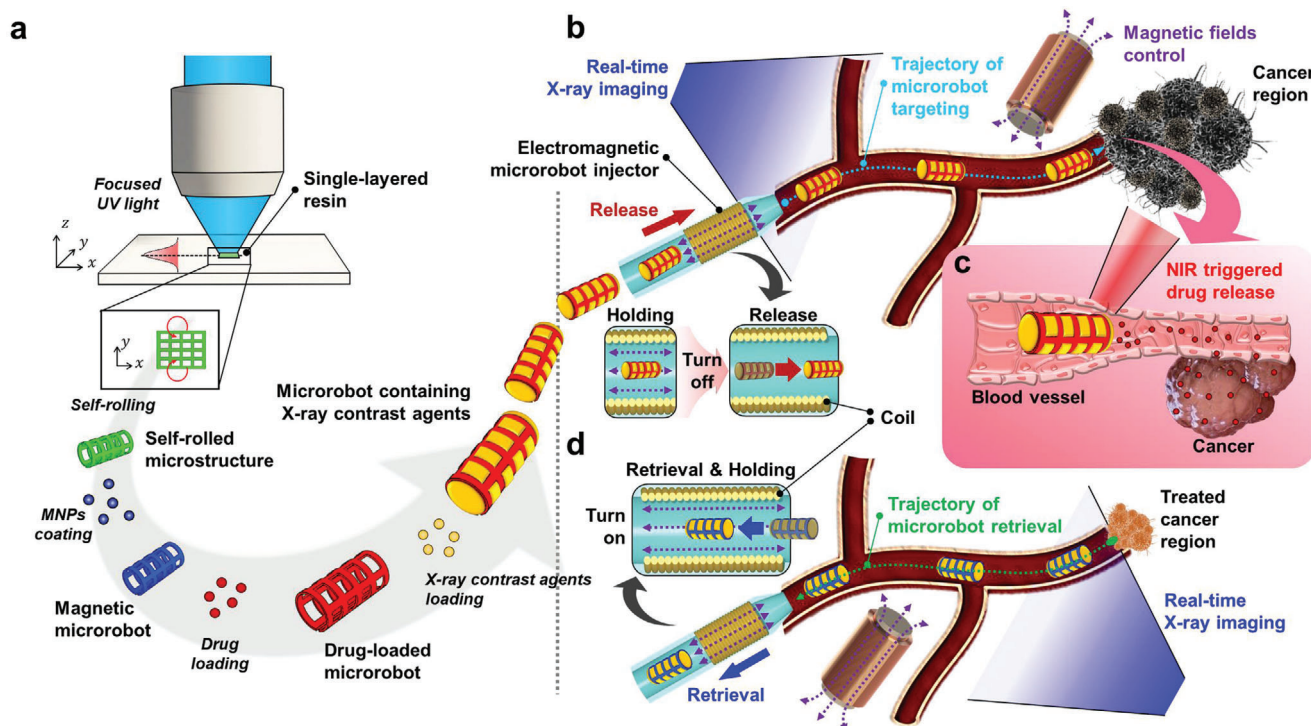


**Figure 1.** Schematic illustration of a magnetically guided self-rolled microrobot for targeted drug delivery, X-ray imaging, and microrobot retrieval. a) Preparation of self-rolled microrobot containing drug and X-ray contrast agent. b) Automated microrobot targeting using magnetic field control of the EMA system and the electromagnetic microrobot injector under real-time X-ray imaging. c) Controlled drug release from the microrobot by NIR stimulus. d) Automated microrobot retrieval using magnetic field control of the EMA system and the electromagnetic microrobot injector under real-time X-ray imaging.

prescribed photon intensity gradient. The self-rolled microrobot with a porous rod shape can support high loads of MNPs and drugs because of its large surface area and also be filled with an X-ray contrast agent. Next, the microrobot surface is covered with MNPs. The MNPs provide magnetic targeting and drug-loading capabilities to the microrobot. Moreover, they enable selective drug release from the microrobot by external stimuli. In addition to the fabrication of a self-rolled microrobot for carrying drugs and X-ray contrast agents, autonomous navigation control of the microrobot was introduced for precise delivery to the lesion site and safe retrieval of the microrobot. This automated microrobot delivery can overcome current microrobotic drug delivery limitations that rely on teleoperation beyond the existing drug delivery using body circulation.

## 2. Results and Discussion

### 2.1. Fabrication of the Self-Rolled Microrobot for Loading of Therapeutic Agents

The microrobot was fabricated through a single-layer-based self-rolling technique and MNP attachment (Figure 1a). First, a self-rolled microstructure for the microrobot body was obtained using focused UV light ( $\lambda = 365 \text{ nm}$ ). The self-rolling of a single material occurs as a product encoded with an anisotropic density gradient along the z-axis generated in the printing process of a single material using focused light with a photon intensity

gradient. The cross-linking gradient of the resin to the z-axis was determined by the UV exposure time. This UV exposure time affects the polymerization of the resin. Based on the bottom of the chamber, the resin gradually polymerizes along the z-axis, and is divided into hard and soft layers. In this polymerized resin, the hard layer becomes thicker than the soft layer as the UV exposure time increases. To prove this hypothesis, we observed the self-rolling behavior of the polymerized structure by the cross-linking gradient according to the UV exposure time. As a result, we confirmed that the curvature of the polymerized structure gradually increases with the increase of the UV exposure time (Figure S1, Supporting Information). This result means that the self-rolling behavior decreases as the hard layer becomes thicker than the soft layer in the polymerized resin due to the increase in UV exposure time. This self-rolling technique using focused UV light enabled fabrication of a rod-shaped microrobot for demonstrating in vitro autonomously navigated drug delivery (Figure 2a). Shape morphing in the material printed using the focused UV light is isotropic because it originates from the density difference between the top and bottom layers, and the contraction of the top layer is isotropic (without structure; see the upper row in Figure 2a). When a material is printed without a pattern, shape morphing is limited to formation of a bowl shape, in which the center sinks while the edges rise, owing to the existence of upward-facing isotropic torque ( $\tau$ ). Therefore, we introduced an asymmetric pattern to enable shape-morphing to the desired rod shape, which has low fluid resistance as well as

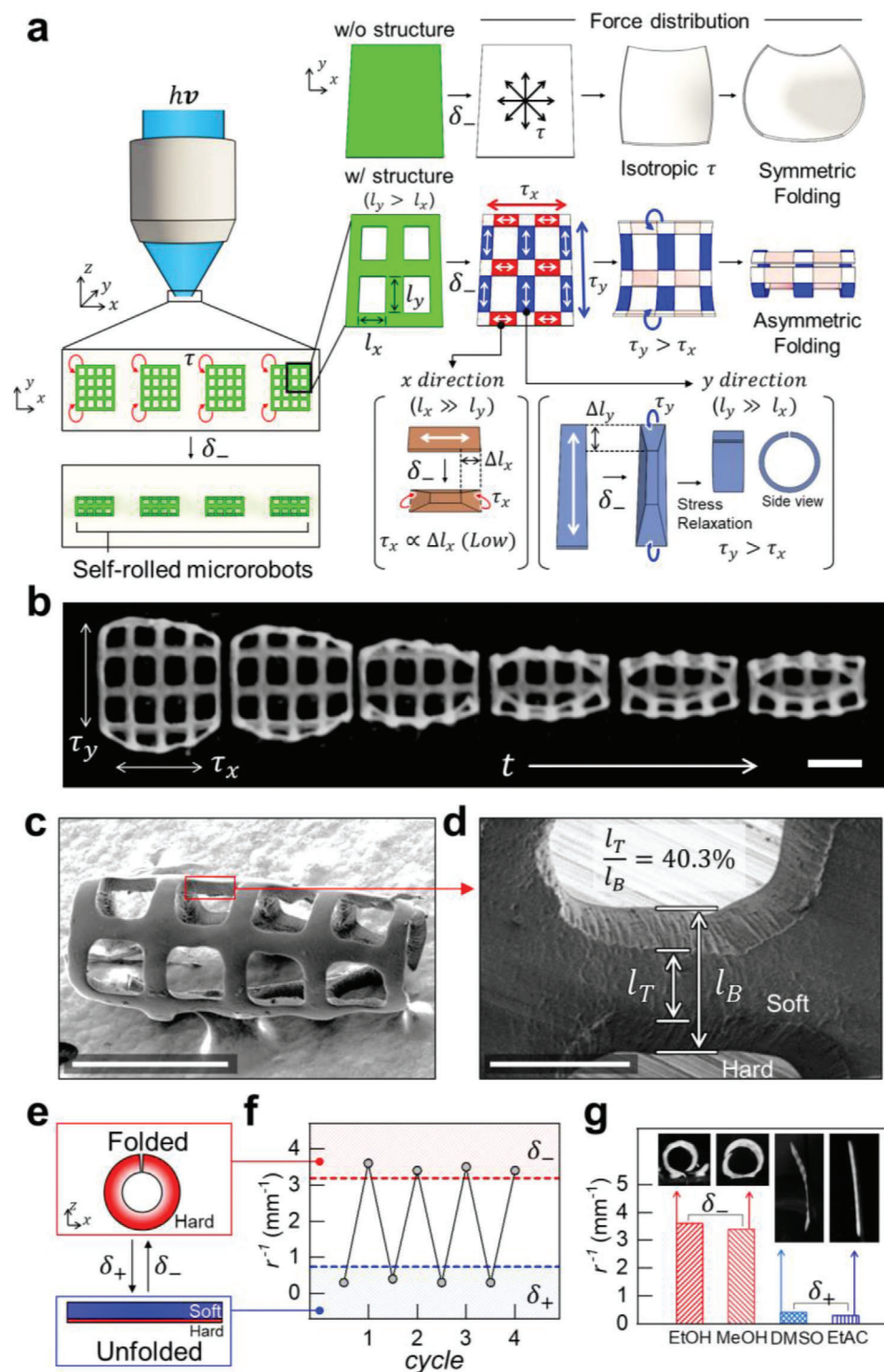


**Figure 2.** Fabrication and characterization of the self-rolled microstructure. a) Schematic illustration of the mechanism of asymmetric folding for the fabrication of a rod-shaped microrobot ( $r = 250 \mu\text{m}$ ). Shape morphing of the self-rolled single layer is isotropic because shape-morphing originates from the density difference between the top and bottom layers (upper row; without structure). Therefore, the asymmetric pattern is introduced to enable shape-morphing to the desired rod shape (lower row; with structure). When the length of one direction ( $x$  or  $y$ ) is significantly larger than the other (e.g.,  $l_x > 5l_y$ ), the length contracted during shape-morphing along the longer direction ( $\Delta l_x$  or  $\Delta l_y$  in the inset) is significantly greater than that of the counterpart. This results in an asymmetric shape-morphing along the longer direction because the torque ( $\tau_x$  or  $\tau_y$  in the inset) is greater than that of the other direction. b) Time-dependent optical microscope image of the printed material with an asymmetric pattern (scale bar:  $500 \mu\text{m}$ ). Upon protic stimulation, shape-morphing occurs along the  $y$  direction over time because  $\tau_y$  is greater than  $\tau_x$ . It then transforms into a cylindrical asymmetric

high drug-loading capacity (with structure; see the lower row of Figure 2a). If the length in one direction ( $x$  or  $y$ ) is significantly greater than that in the other (e.g.,  $l_x > 5l_y$ ), the length contracted during shape morphing, along the longer direction ( $\Delta l_x$  or  $\Delta l_y$  in the inset), is significantly greater than that of the counterpart. Therefore, asymmetric shape-morphing occurs along the longer direction because the torque ( $\tau_x$  or  $\tau_y$  in the inset) is higher than that in the other direction. Therefore, the force distribution during shape-morphing can be simplified, with parts receiving only  $x$ -axis torque ( $\tau_x$ , red), parts receiving only  $y$  axis torque ( $\tau_y$ , blue), and parts that are isotropically folded ( $\tau$ , white). As a result, if the length in one direction ( $l_y$ ; blue) is greater than that in the other ( $l_x$ ; red) ( $l_y > l_x$ ), asymmetric shape morphing along the longer direction ( $y$ ) occurs. Figure 2b shows a time-lapse optical microscope image of the asymmetric folding of focused UV-light-printed material (see also Movie S1, Supporting Information). Initially, the printed material is in a mesh-shaped 2D form. As protic stimuli are applied, shape morphing occurs along the  $y$  direction over time, owing to  $\tau_y$ . Subsequently, transformation into a cylindrical asymmetric structure occurs. In the last image, the tip is not entirely closed owing to the existence of  $\tau_x$ . Furthermore, repeatability for the formation of self-rolled microstructures was carried out in several microrobots. As a result, all single layers were transformed into rod shapes by the proposed focused UV light polymerization (see also Movie S1, Supporting Information). Therefore, these results show that the proposed a single-layer-based self-rolling technique can be performed stably and repeatedly in the fabrication of microrobots. Figure 2c shows a scanning electron microscope (SEM) image of the asymmetric structure with a radius of 250  $\mu\text{m}$  after shape morphing. Figure 2d shows the shape-morphed asymmetric structure observed from the top layer. The length of the top layer ( $l_T$ ) is clearly less than the length of the bottom layer ( $l_B$ ) because it shrinks by forming a soft layer ( $l_T/l_B \approx 40\%$ ). Moreover, the surface of the bottom layer is smooth, whereas the surface of the top layer is rough and has wrinkles owing to the shrinkage occurring exclusively in the top layer (Figure S2, Supporting Information). Furthermore, the existence of both hard and soft layers enabled reversible and repeatable shape morphing of the printed material under protic or aprotic stimuli (see Figure 2e and Movie S2, Supporting Information). With protic stimuli, the surface energy of the printed material is increased to fold printed material by condensation of the soft layer, whereas in an aprotic solvent, the surface energy of the printed material is decreased to unfold printed material. The folding and unfolding are reversible and repeatable upon the application of repeated protic (red) and aprotic (blue) stimuli (Figure 2f). In this demonstration, ethanol was used to apply protic stimuli, and dimethyl sulfoxide (DMSO) was used to apply aprotic stimuli. Also, the shape-morphing property using various protic solvents (ethanol and methanol; red) and aprotic solvents (DMSO and ethyl acetate; blue) was also demonstrated (Figure 2g).

Next, to apply the asymmetric structure needed for a mobile microrobot to be moved by using an electromagnetic actuation (EMA) system, MNPs and the anticancer drug (doxorubicin, DOX) were loaded onto the surface of the microrobot (Figure 3a). The surface of the microrobot was first coated using polydopamine (PDA) to covalently link amine-functionalized MNPs via Schiff-base linkage, while DOX was noncovalently attached via hydrogen bonding.<sup>[48]</sup> Upon thermal perturbation, using a NIR laser, DOX is released, while MNP remains on the microrobot owing to the covalent bonding. The detailed procedure is described in the Experimental Section. The energy dispersive spectroscopy mapping image shown in Figure 3b shows the morphological structure of the microrobot, obtained using the secondary electron, and the distribution of two elements (O and Fe). O and Fe uniformly coexist in the microrobot. This result indicates that the MNPs and DOX were uniformly loaded onto the surface of the microrobot. The MNPs exhibited a suitable magnetization value ( $M_{\text{sat}} \approx 40 \text{ emu g}^{-1}$ ) for operation using the EMA system with superparamagnetic properties (Figure 3c). After assembly of MNPs on the asymmetric microrobot, the magnetization value of the asymmetric microrobot was about one-fourth that of the bare MNPs, a result similar with that of our previous report.<sup>[49]</sup> DOX loading was also optically demonstrated as its  $\pi$  electron absorption peak ( $\lambda \approx 480 \text{ nm}$ ) was observed in the DOX-loaded microrobot (number 2), but it was not observed in the bare microrobot (number 1) (Figure 3d). Next, drug loading on the magnetic microrobot was investigated according to the DOX concentration. As a result, as the DOX concentration increased, the drug carried on the microrobot gradually increased (Figure S3, Supporting Information). The continuous increase in the amount of drug loading without saturation shows that the magnetic microrobot has sufficient space to load the drug regardless of the attachment of MNPs.

For NIR-laser-triggered drug release application of asymmetric microrobots, photothermal heating of the microrobot was evaluated (Figure 3e). Upon NIR laser irradiation (808 nm and 5  $\text{W cm}^{-2}$ ), the temperature elevation ( $\Delta T$ ) in the vicinity of the microrobot rose above 16  $^{\circ}\text{C}$  within 80 s. This value is enough to release DOX from the microrobot's surface.<sup>[50,51]</sup> It is notable that, although MNPs do not exhibit strong light absorption in the NIR region, previous studies have reported that clustered MNPs exhibit fairly acceptable photothermal heat generation owing to the clustering effect.<sup>[50,52,53]</sup> NIR-triggered DOX release from the microrobot is demonstrated in Figure 3f,g. Because the region around the tumor is acidic as the result of cancer cell metabolism, the DOX release experiment was performed at Phosphate-buffered saline (PBS) buffer with three different pH values (5.0: red, 6.0: green, and 7.4: blue).<sup>[50,54,55]</sup> First, time-dependent autonomous DOX release from the microrobot was measured to investigate the premature release of DOX before NIR laser triggering (Figure 3f). The DOX molecules were spontaneously released without NIR laser irradiation, owing to the

structure. c) Perspective view (scale bar: 500  $\mu\text{m}$ ) and d) enlarged top view (scale bar: 100  $\mu\text{m}$ ) SEM image of the cylindrical asymmetric structure after shape-morphing. The length of the top layer (IT) is obviously less than that of the bottom layer (IB) because the top layer shrinks by forming a soft layer ( $IT/IB \approx 40\%$ ). e) Schematic illustration of the folding and unfolding of the printed material upon aprotic ( $\delta+$ ) and protic ( $\delta-$ ) stimuli. f) Reversible deformation and recovery of the printed material upon repeated protic ( $\delta-$ ; red) and aprotic ( $\delta+$ ; blue) stimuli. Ethanol is used to apply protic stimuli and DMSO is used to apply aprotic stimuli. g) The curvature of the printed materials in various protic (ethanol and methanol; red) and aprotic (DMSO and ethyl acetate; blue) solvents.

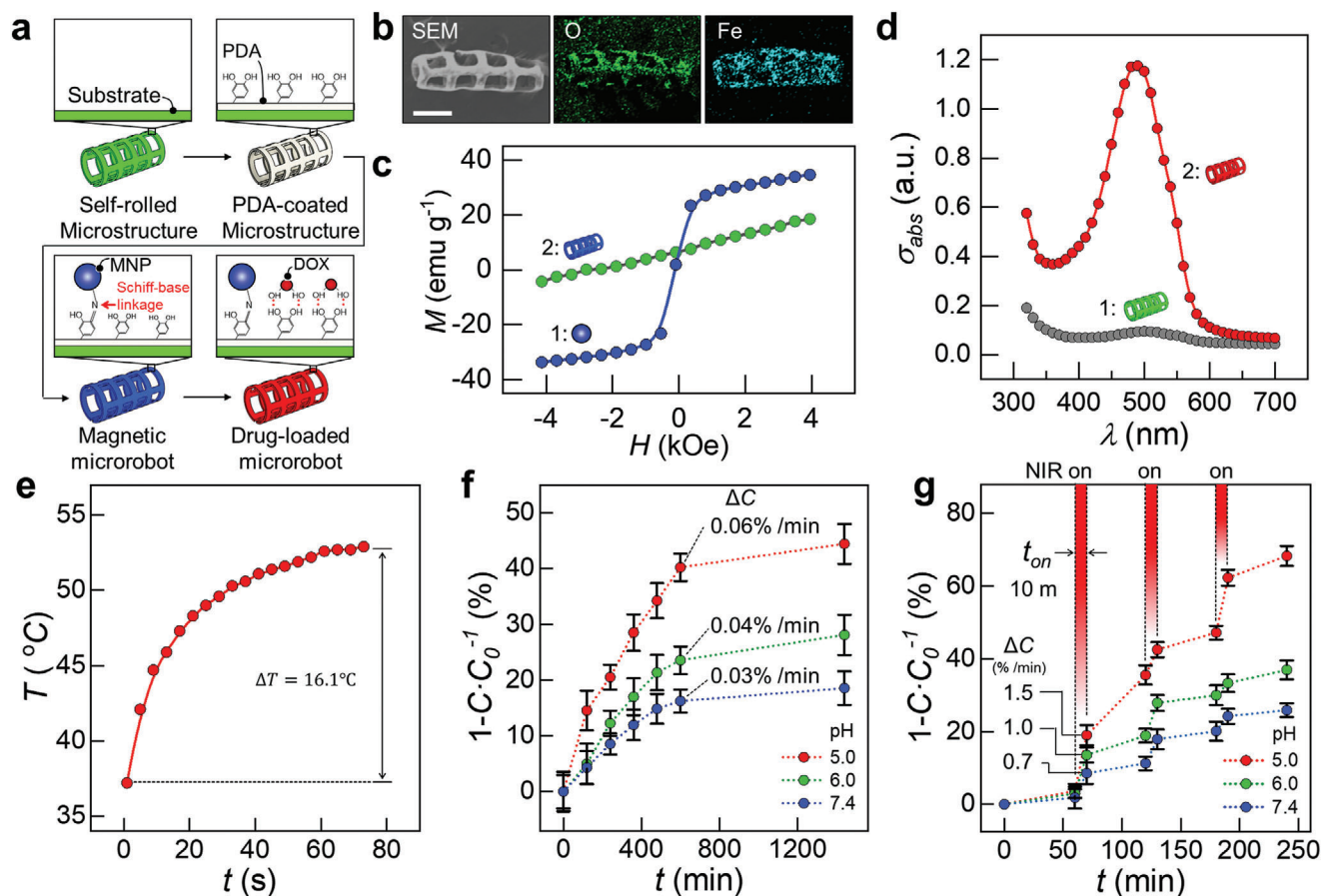


**Figure 3.** Fabrication and characterization of the drug-loaded magnetic microrobot. a) Schematic illustration of MNP and anticancer drug-loading procedure. b) Energy dispersive X-ray spectroscopy mapping image of the cylindrical asymmetric structure after MNP and DOX loading (scale bar: 500  $\mu m$ ). c) Magnetic hysteresis loop of the MNPs (number 1; blue) and asymmetric microrobots (number 2; green). The MNPs exhibit a suitable magnetization value ( $M_{sat} \approx 40$  emu  $g^{-1}$ ) for operation using the EMA system with a superparamagnetic property. d) Light absorption spectrum of the bare microrobot (number 1; gray) and microrobot after MNP and DOX loading (number 2; red). The absorption peak of DOX ( $\lambda \approx 480$  nm) is observed in the DOX-loaded microrobot. e) Time-dependent photothermal heating profile of the microrobot under NIR laser irradiation (808 nm and  $5 W cm^{-2}$ ). f) Time-dependent DOX release from the microrobot in the PBS buffer at various pH values (red = 5.0, green = 6.0, and blue = 7.4). g) NIR-triggered DOX release from the microrobot under repeated periodic (on: red; off: white) NIR laser irradiation (808 nm and  $5 W cm^{-2}$ ) in the PBS buffer at various pH values (red = 5.0, green = 6.0, and blue = 7.4).

relatively weak bonding between DOX and the microrobot ( $0.06\% min^{-1}$  at pH = 5.0,  $0.04\% min^{-1}$  at pH = 6.0, and  $0.03\% min^{-1}$  at pH = 7.4). These amounts are not significant at our time scale. In contrast, under NIR laser irradiation ( $808 nm$  and  $5 W cm^{-2}$ ), significant amounts of DOX molecules were released ( $1.5\% min^{-1}$  at pH = 5.0,  $1.0\% min^{-1}$  at pH = 6.0, and  $0.7\% min^{-1}$  at pH = 7.4), as shown in Figure 3g. Upon NIR laser irradiation, DOX was released owing to the local heating around the microrobot by photon-to-phonon conversion.<sup>[56]</sup> It is notable that the DOX release rate at lower pH is higher than that at higher pH because of the protonation of the amino group in the DOX molecule.<sup>[50,54]</sup> In vivo drug-loaded microrobot targeting situation, when the DOX-loaded microrobot is injected through the catheter in the blood vessel, the released drug before microrobot targeting induces side effect due to diffusion of the drug from the microrobot. Fortunately, because the DOX-loaded microrobot is delivered to the target blood vessel within few seconds to minutes, the drug released from the microrobot is less than 1% of

the total amount calculated by the drug release results. As a result, since the amount of drugs released during the delivery of the microrobot is minimal, the microrobot can deliver most of the loaded drug to the lesion without loss.

## 2.2. Targeted Delivery of the Microrobot Using Autonomous Driving Control

Various microrobot-aided drug delivery systems have the advantage that the drug can be released near the tumor with a higher concentration than that of a conventional drug delivery system.<sup>[19,57]</sup> However, most microrobot systems use degradable polymers, which allow the microrobot to dissolve over time, after releasing the drug near the tumor. This approach has two critical disadvantages. The first is that the biodegradation of the microrobot takes a long time ( $\approx 1$  week). This hinders the retreatment of drugs because the used microrobot occupies the blood vessel

adjacent to the tumor.<sup>[58]</sup> The second is that the degraded material affects the surrounding environment, such as by raising the pH or disrupting ionic balance. Therefore, to solve this problem, we have developed an automated microrobotic drug delivery system that integrates microrobot injection, navigation, drug release, and retrieval (Figure 1). To demonstrate the proof of concept of autonomously navigated microrobot-based drug delivery, we used a magnetic guidance system. The microrobot moves automatically along the generated trajectory, via an EMA system, with respect to the recognized location of the microrobot, using a charge-coupled device (Figure 4a). The microrobot is autonomously driven from the starting location (denoted as S) to the target location (denoted as T) using the EMA system (number 1). Thereafter, the drug is released upon irradiating the microrobot with the NIR laser (number 2) and the microrobot returns to the starting location (number 3). Figure 4b depicts an EMA system for the autonomous driving and drug release. The flowchart of the autonomous navigation system is depicted in Figure 4c. Highly accurate, stable positioning of the microrobot is achieved by adopting feedback control using a computer vision tracker. The position closed-loop control is handled by the proportional-integral-derivative (PID) position controller, with a tracked position from the camera place on top of the workspace. After generation of the desired trajectory using a preoperative image, the location of the microrobot is recognized by a vision tracker. Then, after the current location is compared with the generated trajectory, the desired magnetic field is calculated using the PID position controller. The microrobot autonomously moves according to the magnetic field, which is generated by the EMA system. The current in each coil in the EMA system is determined according to Equation (1).

$$I = \begin{bmatrix} B(C) \\ M^T \partial B_x(C) \\ M^T \partial B_y(C) \\ M^T \partial B_z(C) \end{bmatrix}^\dagger \begin{bmatrix} B \\ F \end{bmatrix} \quad (1)$$

The unit-current matrices  $B(C)$ ,  $\partial B_x(C)$ ,  $\partial B_y(C)$ , and  $\partial B_z(C)$  are calculated from the simulation model. First, the proposed control scheme is used to autonomously control the microrobot in an in vitro environment. A microfluidic channel mimicking a human portal vein (HPV) was prepared to demonstrate in vitro autonomous navigation from the starting position (S) to three target positions (T1, T2, and T3). Autonomous navigation of the microrobot using the EMA system is depicted in Figure 4d and Movie S3, Supporting Information. First, two microrobot trajectories for navigating to target location T2 (P1, blue line) and returning to the initial location (P2, green) were generated with inputs from user selection. Thereafter, the computer vision tracker recognized the location of the microrobot. Based on the PID controller's calculation, a magnetic field is generated to induce gradient pulling motion to navigate the microrobot to the desired location. Figure 4e shows the tracked positions of the microrobot along the given path (S→T2→S). The tracking results indicate that the microrobot was well controlled, tracing the path with a maximum root mean square error of  $106.75 \pm 105.46 \mu\text{m}$  with respect to the  $y$ -axis (as shown in Figure 4f). In addition, the tracking results of the microrobot moving to T1 and T3 can be found in Figure S4, Supporting Information. In the gradient pulling mo-

tion, the magnitude of the magnetic field gradient induced the magnetic force exerted on the microrobot to dominate its translational velocity. The movement of the microrobot using the EMA system with respect to the various magnetic field gradients ( $0.2\text{--}1.2 \text{ T m}^{-1}$ ) was investigated, and the results are shown in Figure 4g. The self-rolled microrobot (number 1; red) exhibited a higher speed than the planar microrobot (number 2; gray). Moreover, the self-rolled microrobot had a suitable velocity for drug delivery applications via the EMA system ( $v \approx 5 \text{ mm s}^{-1}$ ).

In this study, we showed that one microrobot could be loaded with maximum of  $15.8 \mu\text{g}$  of DOX, which showed a tumor-killing effect in an in vitro test. Considering animal experimental stage, the general dose range is between  $1\text{--}5 \text{ mg kg}^{-1}$ .<sup>[59,60]</sup> Let us consider the mouse model, which weight about  $30\text{--}70 \text{ g}$ . Therefore, the amount of  $5\text{--}10$  microrobots need to be injected into the body to deliver a sufficient amount of drugs to tumors. As a feasibility test for delivery of multiple microrobots, we performed swarm motion of the  $5\text{--}10$  microrobots through the magnetic field control of the EMA system in a  $5 \text{ mm}$ -width 3D-printed channel filled with PBS solution (as shown in Figure S5, Supporting Information). Under applied magnetic field, the microrobots are aggregated into a random shape thanks to the dipole-dipole interaction forces and swarm together to reach the target point. It obvious that the swarm structures of  $5$  or  $10$  microrobots can maintain their shape during the locomotion, which demonstrated that these magnetic interaction force between the microrobots are relatively higher than the drag force exerted on each robot (see Movie S4, Supporting Information, for more details).

In order to investigate the effect of the blood flow on the microrobot performance for in vivo, the microrobot's performance inside a dynamic fluidic channel will be recorded and analyzed as shown in Figure 4h. A fluidic channel,  $5 \text{ mm} \times 20 \text{ mm}$ , is fabricated using the 3D printer, as shown in Figure 4h. The flow rate is controlled by the multichannel syringe pump (Fusion 4000, Chemyx, USA). To investigate the effects of the flow to the locomotion of the microrobot, three different motion conditions are considered with a variable flow rate ranging from  $1$  to  $4 \text{ mL min}^{-1}$ , including the upstream motion, downstream motion without magnetic force, and downstream motion with applied magnetic force as shown in Figure 4h (see also Movie S5, Supporting Information, for more details). The magnetic field applied in these experiments is  $40 \text{ mT}$ ,  $1.3 \text{ T m}^{-1}$ . Obviously, the locomotion speed of the microrobot in downstream motion with and without magnetic force (illustrate as a blue dashed line and green solid line in right of Figure 4h) gradually increases with the increase of the flow rate. Interestingly, the increment of microrobot's moving speed of these two motions has almost the same rate. The gaps between these two lines in different flow rates are varied from  $5.2\text{--}6.3 \text{ mm s}^{-1}$ , which are the contributions of the magnetic force. Here, despite the moving velocity decrease with the increment of flow rate, the microrobot demonstrates its upstream motion capability. Consequently, this result illustrated the possibility of microrobot retrieval proposed in this work.

Real-time imaging of microrobots using X-rays has been regarded as a challenging issue for microrobot systems for drug delivery because of the low density of microrobots and high permeability of X-rays because of their small size. To solve this limitation, we loaded Lipiodol, known as a representative X-ray contrast medium, into the microrobot. In general, Lipiodol forms

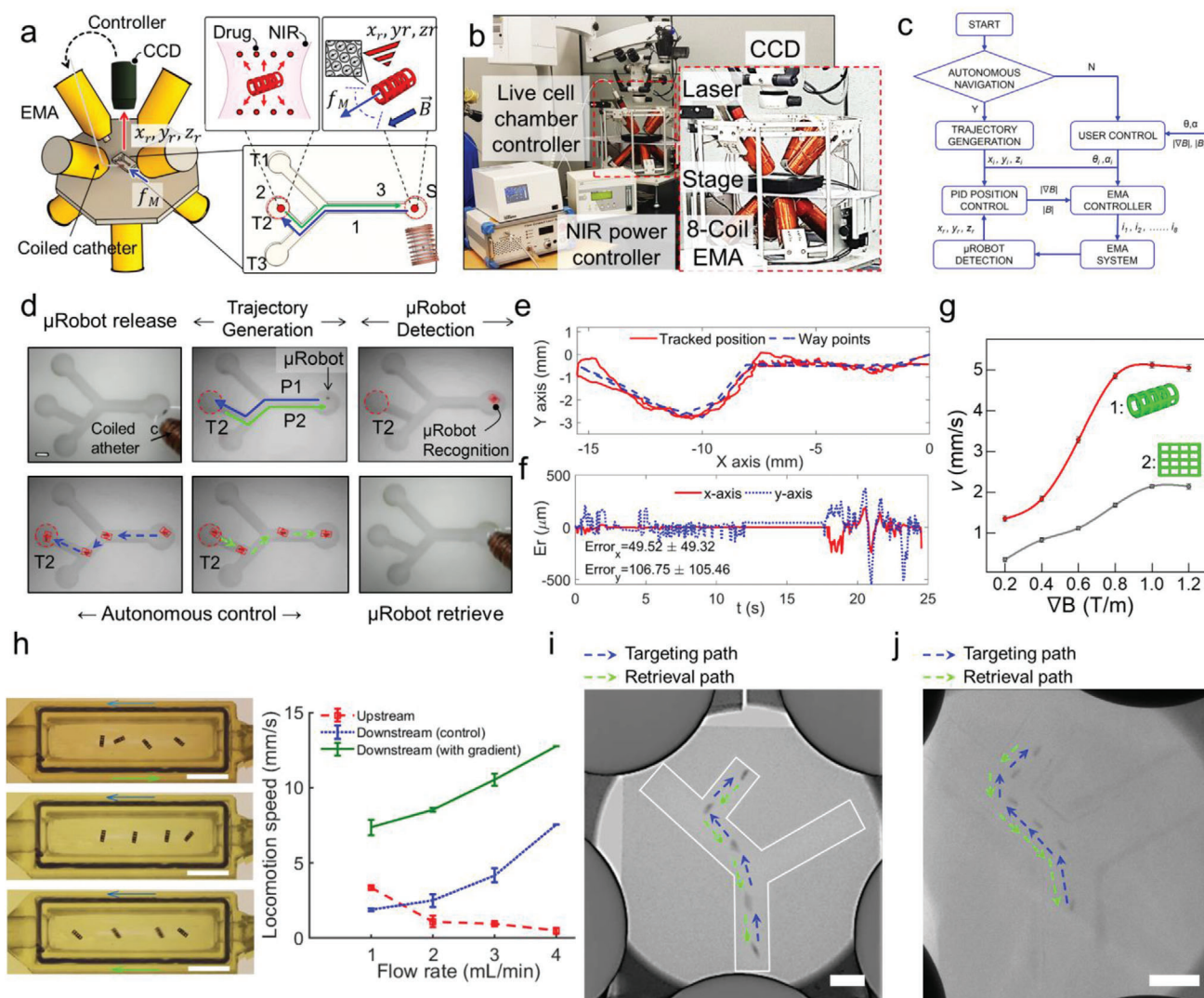


**Figure 4.** Autonomous navigation of the microrobot using an EMA system. a) Schematic illustration of an autonomously navigated microrobot-based drug delivery system, which automatically moves the microrobot to the generated trajectory, using an EMA system, with respect to the recognized location of the microrobot, using a charge-coupled device (CCD) sensor. The microrobot is first released from the coiled catheter and autonomously driven from the starting location (S) to the target location (T) using the EMA system (number 1). Thereafter, the drugs are released by irradiating the microrobot with the NIR laser (number 2); it then returns to the starting location (number 3). Finally, the microrobot is retrieved using the coiled catheter. b) Digital photograph of an integrated EMA system for autonomous driving and drug release. c) Flowchart of the software structure for the proposed system that can operate in both autonomous navigation mode and manual mode. In the autonomous navigation mode, the location of the microrobot is recognized by a vision tracker after generating the desired trajectory. Then, after comparing the current location with the generated trajectory, the desired magnetic field is calculated by the PID position controller. The microrobot is moved to the next differential position according to the magnetic field, which is generated by the EMA system. This feedback logic is repeated until the microrobot reaches the desired position. d) Sequential optical microscopy image of a microrobot located in the *in vitro* fluidic channel, demonstrating autonomous navigation using the EMA system (scale bar: 1 mm). After the trajectory generation, the computer vision tracker recognizes the location of the microrobot (red square box). Then, the microrobot is autonomously navigated to the desired location by the magnetic field, which is generated to induce translational as well as rotational motion. Release and retrieval of the microrobot are accomplished by the self-built coiled catheter. e) Tracked position of the microrobot in the 2D vessel phantom. f) The root-mean-square tracking errors are calculated in both the x and y axes with respect to the desired way points and tracked position of the microrobot. g) Velocity distribution of the rod-shaped microrobot (number 1; red) and planar microrobot (number 2; gray) using the EMA system with respect to various gradient magnetic field intensities (0.2–1.2 T m<sup>-1</sup>). h) Effects of flow to the performance of microrobot locomotion in (the top figure on the left) upstream direction, (middle figure on the left) downstream direction without magnetic force, and (bottom figure on the left) downstream direction with magnetic force (40 mT, 1.3 T m<sup>-1</sup>). Figure on the right: Dependence of microrobot's locomotion speed with various flow rate (1, 2, 3, 4 mL min<sup>-1</sup>) in three aforementioned conditions. The blue arrows are the flow direction, and green arrows are the orientation of the applied magnetics force. The scale bars are all 5 mm. i) Time-lapse X-ray image demonstrating the motion of the microrobot in the 2D vessel phantom (scale bar: 5 mm). The white contour is the channel outline. j) Time-lapse X-ray image with a thick layer of pork meat on top of the channel demonstrating the motion of the microrobot in the 2D vessel phantom (scale bar: 5 mm).

an emulsion with a water-based solution as an oil-based X-ray contrast and is injected into the blood vessel.<sup>[61,62]</sup> Using the iodized oil property, the Lipiodol-loaded microrobot can be observed in real-time through X-ray imaging during targeting and retrieval because of the unique hydrophobic properties of Lipiodol (Figure 4i). In order to verify the visibility of the microrobot under real-time X-Ray for in vivo, a thick three-layer pork meat was placed on top of the 3D printed channel. (See Figure S6a,b, Supporting Information, for additional details of this experimental setup.) Figures 4i and 4j show the X-ray time-lapse images of the microrobot motion-controlled along the aforementioned (S→T2→S) path without and with a thick layer of meat on top of the channel, respectively. Additional X-ray images of microrobot motion along different paths are detailed in Figure S6c–f and Movies S6 and S7, Supporting Information. These experimental results illustrate that the proposed microrobot can be clearly observed under X-ray imaging. Furthermore, X-ray imaging of the microrobot with and without meat was evaluated through the grayscale intensity of the image (Figure S6g, Supporting Information). From the X-ray image and the extracted intensity values, the Lipiodol-loaded microrobot is clearly distinguished from the PBS-filled channel in both conditions. In addition, there is little difference in the grayscale intensity of the Lipiodol-loaded microrobot with and without meat. As a result, the microrobot can stably perform targeted drug delivery and be retrieved under real-time X-ray imaging without loss of Lipiodol from the microrobot. This visualization test demonstrates the possibility of the X-Ray real-time imaging for in vivo in a future application.

### 2.3. In Vitro Cellular Drug Delivery Using the Magnetically Guided Microrobot

We demonstrated in vitro cellular drug delivery using the magnetically guided microrobot (Figure 5a). The therapeutic efficacy of microrobots was evaluated by using Hep3B cells containing the HPV-mimicking channel. A microrobot was autonomously navigated to the target location, where a Hep3B-cell-containing membrane was located. Subsequently, the region was irradiated for 10 min with an NIR laser to induce apoptosis of Hep3B cells (Figure 5b). The NIR irradiation increased the temperature of the microrobot, and the DOX molecules were released after breaking of weak hydrogen bonding by thermal perturbation. Thereafter, the DOX molecules were internalized in cancer cells by diffusion. Finally, DOX molecules were internalized in the cell nuclei, where they induce apoptosis. The internalization of the DOX molecules into a cell nucleus is visualized using fluorescent microscopy (Figure 5c). Neither a chamber without a microrobot nor one targeted with a microrobot without DOX molecules exhibit the characteristic red fluorescence originating from the DOX molecule. A chamber targeted with a DOX-loaded microrobot ( $C_{\text{DOX}}$ : 3.3  $\mu\text{g}$  per one microrobot) exhibited ambiguous red fluorescence from the auto release of the DOX molecule. However, after NIR laser irradiation (808 nm and 5 W  $\text{cm}^{-2}$ ) for 10 min, the red fluorescence was distinctively enhanced in the cell nucleus. This result supports the conclusion that the NIR laser irradiation is effectively triggering the release of DOX molecules. It is notable that, under NIR laser irradiation, the release rate of DOX molecules at pH = 7.4 is 0.7% per min. Therefore, 0.7  $\mu\text{g}$  of DOX

molecules (21% of the initial amount of DOX) is arithmetically expected to be released.

Finally, the in vitro therapeutic effect of our targeted drug delivery using an asymmetric microrobot with respect to drug concentration ( $C_{\text{DOX}}$ ; Figure 5d) and various numbers of microrobots ( $N_R$ ; Figure 5e) was demonstrated by using a 3-(4,5-dimethylthiazol-2-yl)-2,5-diphenyltetrazolium bromide assay. Comparison of the cellular viability of cells without (gray bars) and with (green bars) the bare asymmetric microrobot reveals no significant difference in cytotoxicity, indicating good biocompatibilities of the asymmetric microrobot. However, after targeting of the DOX-loaded microrobot (blue bars), cellular viability monotonically decreased as  $C_{\text{DOX}}$  or  $N_R$  was increased as a result of the autorelease of loaded DOX. Moreover, after NIR laser triggering to the DOX-loaded microrobot (red bars), further distinguishably reduced cellular viability was demonstrated. Combined with the coiled catheter, which is capable of releasing and trapping the microrobot using an electromagnetic field, our EMA system enables autonomously navigated microrobot-based drug delivery. The entire process, which includes microrobot release, autonomous navigation, and microrobot retrieval using the EMA system, is detailed in Movie S3, Supporting Information. Our results indicate that the proposed magnetically guided self-rolled microrobot has the capability to overcome the current primary issue, that is, retreatment using the microrobotic drug delivery system.

### 3. Discussion

In this study, we performed targeted drug delivery using a magnetically guided self-rolled microrobot. The proposed microrobot was designed and fabricated by considering targeted drug delivery under X-ray imaging and retrieval of a microrobot after its delivery. First, the microrobot consisting of a single-layer-based self-rolled body and an MNP-attached surface was loaded with both the drug and an X-ray contrast agent for cancer treatment and real-time X-ray imaging, respectively. Next, magnetic targeting of the prepared microrobot was performed by autonomous driving through magnetic field control of the EMA system. Here, injection and retrieval of the microrobot were conducted using a coiled catheter. After magnetic targeting of the microrobot was performed, controlled drug release from the microrobot was confirmed through NIR triggering, and the therapeutic effect of the released drug was verified through an in vitro test. Although the proposed microrobot has been verified through several experiments encompassing microrobot autonomous targeting control, controlled drug delivery, and safe retrieval, there are some issues that need to be explored further before clinical trials can be conducted.

Most studies of microrobots for drug delivery have focused on the delivery, implantation, and degradation of the microrobots to target sites. Currently, several studies have demonstrated that targeted drug delivery using magnetic driving and biodegradation of microrobots are possible through in vitro and in vivo experiments.<sup>[15–21,63]</sup> However, because the microrobots are in direct contact with tissue, local toxicity can be induced.<sup>[15,22]</sup> In addition, the degraded products of the microrobot can cause an inflammatory reaction through a pH change in the body. However, because the proposed microrobot can be recovered after

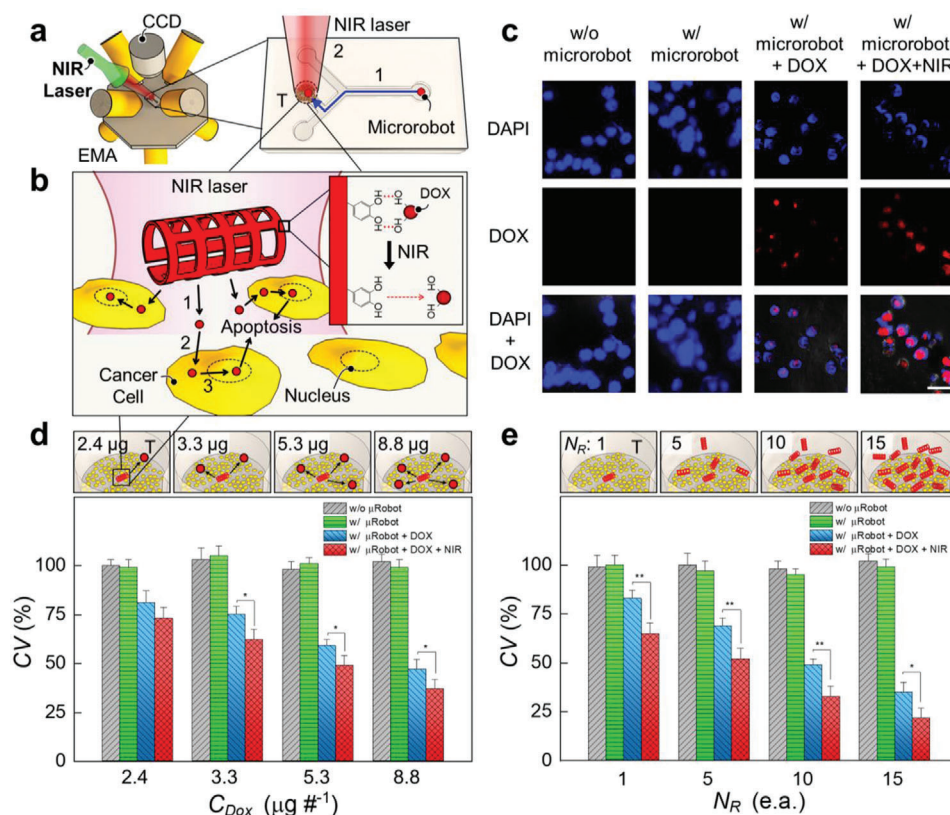


**Figure 5.** In vitro cellular drug delivery using a magnetically guided self-rolled microbot. a) Schematic illustration of targeted drug delivery of the microbot, which performs autonomous navigation using the EMA system and light-triggered drug release using an NIR laser. The microbot is autonomously driven from the starting location to the target location (T) using the EMA system (number 1) and the drugs are released by irradiating the microbot with the NIR laser (number 2). b) Schematic illustration of the cellular apoptosis induced by light-triggered drug release. Upon NIR irradiation, the temperature of the microbot is increased, and the DOX is released after breaking the weak hydrogen bonding by thermal perturbation (number 1). Thereafter, the DOX is internalized in cancer cells by diffusion (number 2). Finally, the DOX is internalized in the cell nucleus, where it induces apoptosis (number 3). c) Visualization of in vitro cellular drug delivery using an integrated drug delivery system. The asymmetric microbot is navigated to the target chamber (denoted as T), where the Hep3B cells are located. Each DOX-loaded microbot is loaded with  $10 \mu\text{g}$  of DOX molecules. After NIR laser ( $808 \text{ nm}$  and  $5 \text{ W cm}^{-2}$ ) irradiation for 10 min, the Hep3B-cell-containing membrane is imaged using fluorescence microscopy (scale bar:  $100 \mu\text{m}$ ). A strong red fluorescence originated by the DOX molecule is observed in the nucleus. d)  $C_{Dox}$ -dependent in vitro cellular viability test of Hep3B cells located in the target chamber (denoted as T) after the autonomous navigation of an asymmetric microbot without (green bar) and with (blue bar) DOX. Thereafter, the area is irradiated with an NIR laser ( $808 \text{ nm}$  and  $5 \text{ W cm}^{-2}$ ) for 10 min (red bar) ( $*P < 0.05$ , Student's  $t$  test;  $n = 3$ ). e)  $N_R$ -dependent in vitro cellular viability test of Hep3B cells located in the target chamber (denoted as T) after the autonomous navigation of an asymmetric microbot without (green bar) and with (blue bar) DOX. Thereafter, the area is irradiated with an NIR laser ( $808 \text{ nm}$  and  $5 \text{ W cm}^{-2}$ ) for 10 min (red bar) ( $**P < 0.01$  and  $*P < 0.05$ , Student's  $t$  test;  $n = 3$ ).

NIR-triggered drug release, concerns about the toxicity of biodegradable materials can be resolved. Despite the advantages of these recoverable microrobots, microrobots have the potential to induce reactions with the immune system upon injection into the body. In addition, depending on the environment and flow rate of the biofluid and external stimulus for controlled drug release, loosely attached MNPs or parts of the microstructure may be separated. These separated substances may cause potential toxicity. Therefore, the overall safety of microrobots should be verified through hemocompatibility and platelet and leukocyte activation mechanisms. Furthermore, the biocompatibility of microrobot components needs to be confirmed in the long term through in vivo validation

In terms of driving the microrobot, we have shown that the proposed microrobot can be delivered to the blood vessels around the tumor through the magnetic field control of the EMA system.

However, since the locomotion of the microrobot is performed in a 2D blood vessel phantom, the mobility of the microrobot cannot be guaranteed in a blood vessel having a complex 3D shape. Furthermore, in terms of drug delivery of microrobots, microrobots located in target blood vessels are triggered by external stimuli, boosting the spread of drugs, and helping cancer treatment. However, compared to in vitro tests performed on cell culture plates with an isolated environment, in vivo therapy potentially causes loss of drugs due to surrounding complex environments such as blood flow and vascular morphology. In this study, we showed that one drug-loaded microrobot (max.  $15.8 \mu\text{g}$  of DOX) in an in vitro test showed a tumor-killing effect, but there is a limit to confirming the same tumor-killing effect in vivo. Therefore, many microrobots need to be injected into the body to deliver a large amount of drugs to tumors. In our study, the delivery of many of these microrobots has been verified in

3D-printed channels via swarm motion, but the limited 2D locomotion of microrobots requires further verification and improvement to be applied to in vivo and clinical tests. To overcome this issue of locomotion of the microrobots, in a future study, we will perform locomotion of microrobots in 3D vessel phantom and in vivo model. In addition, the in vivo therapeutic effect of microrobot drug delivery will be performed through an in vivo model with an orthotopic model.

Blood flow may strongly affect the performance of the autonomous control system. In the targeting procedure, the driving force may not be a major problem even with strong surface friction, because the flow in the intra-arterial network is strong enough to act as the main power to propel the microrobot. The magnetic force only needs to steer the robot to the target position. In contrast, when the microrobot returns to the injection point in the retrieval process, a strong driven force is required because the microrobot has to move against the blood flow, which may pose a critical challenge from a clinical viewpoint. A detailed study of robot locomotion against the flow at specific target vessels needs to be investigated. In addition, a swarm control strategy is necessary in cases in which multiple microrobots are needed to carry a certain amount of drug to the target lesion.

#### 4. Conclusion

We developed a magnetically guided self-folded microrobot for autonomous-navigation-based targeted drug delivery, real-time X-ray imaging, and microrobot retrieval. A rod-shaped microrobot printed using a self-rolling technique was able to stably load the drug and the X-ray contrast agent. Precise targeting of the therapeutic-agent-loaded microrobot could be performed using autonomous driving control under real-time X-ray imaging. In addition, the microrobot located at the target site was able to rapidly release the drug through NIR triggering, and the released drug was effective in treating cancer cells. After drug release, the microrobot could be safely recovered through an electromagnetic microrobot injector without risk of loss. As a result, we expect that such a magnetically guided self-rolled microrobot could be a candidate to resolve the current primary issue facing microrobot-based drug delivery systems.

#### 5. Experimental Section

**Materials and Reagents:** All chemical reagents were used without further purification. All solutions were prepared using deionized water with a resistivity of  $\geq 18.2 \text{ M}\Omega \text{ cm}$  at  $25^\circ \text{C}$ . E-Dent 400 solution was purchased from E-vision Tec, Inc. DOX was supplied by Jinhe Bio-Technology (China). FluidMAG-amine nanoparticles (50 nm) were purchased from Chemiecell GmbH (Germany). Dopamine hydrochloride was purchased from Sigma-Aldrich (USA). All other chemicals and organic solvents used were of reagent grade or better.

**Fabrication and Characterization of Microrobot:** To prepare the glass chamber, two pieces of strip-shaped double-sided tape (Nitto, Japan) were taped onto a glass slide to build the parallel walls. Here, the thickness (100  $\mu\text{m}$ ) of the double-sided tape determined the height of the channel. Then, a cover glass ( $22 \times 22 \times 0.1 \text{ mm}$ ) was attached on the double-sided tape to form a chamber with a height of 100  $\mu\text{m}$ . Thereafter, the chamber was filled with resin (E-Dent 400, Envisontec, Germany) by the capillary force, and both ends of the channel were sealed with paraffin wax (Figure S7a, Supporting Information). The resin inside the chamber was pat-

terned using a photomask and visualizing the optical system (Figures S7a and S8, Supporting Information). The chamber was placed into the sample holder and polymerized using a UV LED ( $\lambda = 365 \text{ nm}$ ) with fixed power (12  $\mu\text{W}$ ) through a 10 $\times$  objective lens (NA: 0.30) for 3.2 s. The chamber was then immersed in isopropyl alcohol, and the nonpolymerized resin was removed (Figure S7c, Supporting Information). After a few minutes, the polymerized single layer naturally separated from the cover glass and was self-rolled into the rod type (Figure S7d, Supporting Information).

To apply the asymmetric structure as a mobile microrobot using an EMA system, MNPs and DOX were loaded onto the surface of the self-rolled microstructure. The surface of the microstructure was first coated by using PDA to covalently link amine-functionalized MNPs via Schiff-base linkage, whereas DOX was noncovalently attached via formation of hydrogen bonding. In detail, the microstructure was incubated in a 2  $\text{mg mL}^{-1}$  PDA solution in Tris buffer (10  $\text{mM}$  at a pH of 8.5) for 1 h and washed twice using deionized water.<sup>[64]</sup> The PDA-coated microstructure was then incubated in a 25  $\text{mg mL}^{-1}$  MNP solution in Tris buffer for 2 h. After washing using deionized water, the magnetic microrobot was incubated in various concentrations (5, 10, 15, 20, 30, 40, and 50  $\text{mg mL}^{-1}$ ) of DOX solution in a 1 $\times$  PBS buffer for 24 h. Thereafter, the DOX-loaded microrobot was separated from the free DOX solution by centrifugation (at 12 000 rpm for 3 min). For real-time X-ray imaging of the microrobot, Lipiodol was loaded into the dried microrobot as an oil-based X-ray contrast agent. After a few minutes, the Lipiodol-loaded microrobot was carefully washed using deionized water to remove the non-loaded Lipiodol.

Morphologies of the microrobot were observed using a SEM (SU8010, Hitachi, Japan). Element signals of the microrobot were detected using energy-dispersive X-ray spectrometry. A vibrating sample magnetometer (Model 7404, Lake Shore Cryotronics) was used for the evaluation of the magnetic property of the microrobot and MNPs. UV-vis spectroscopy was performed using a Lambda 25 UV-vis spectrophotometer (PerkinElmer, Boston, MA).

**Control Principle and Experimental Setup of EMA System:** For manipulation of the microrobots in the region of interest (ROI), an EMA system was utilized. Details of the construction of the EMA system can be found on our previous reports.<sup>[20,50,57]</sup> In this work, the gradient pulling motion was chosen for controlling the rod-shaped microrobot. Because it has a large aspect ratio (i.e., the ratio of its longer side to its shorter side is 5:2), the gradient pulling motion (instead of rolling and tumbling motions) is the best means to move this rod-shaped microrobot through small-size vessels.<sup>[65]</sup>

When the microrobot is manipulated with a gradient pulling motion, the translational motion will be the viral contribution to the translational velocity. Therefore, the drag force,  $F_d$ , will dominate the motion of the microrobot when it is translating near a surface. If one assumes that the microrobot is a hollow cylinder moving in a low-Reynolds-number fluid along its long axis, the analytical model of the drag force acting on the microrobot can be found in related refs.<sup>[66,67]</sup> as follows:

$$F_d = 0.5\rho v^2 C_d A \quad (2)$$

where  $\rho$  is the density of the fluid,  $v$  is the translational speed of the microrobot, and  $A$  is the cross-sectional area of the robot. The drag coefficient of the microrobot is a function of Reynolds number,  $Re$ , and the sphericity,  $\psi$ , as follows:

$$\log C_d (Re, \psi) = \log C_d (Re, 1) + P (Re, \psi) \quad (3)$$

with

$$C_d (Re, 1) = \frac{24}{Re} (1 + 0.172Re^{0.657}) + \frac{0.413}{1 + 16300Re^{-1.09}} \quad (4)$$

$$P (Re, \psi) = -0.03874 (1 - \psi) \log Re + 0.09238 (1 - \psi) (\log Re)^2 + 0.06003 (1 - \psi) (\log Re)^3 + 0.01005 (1 - \psi) (\log Re)^4 - 0.003571 (1 - \psi) (\log Re)^5 - 0.005697 (1 - \psi)^2 (\log Re)^5 \quad (5)$$

where the sphericity of the hollow cylinder applied in this microrobot, which is the ratio between a spherical surface and the hollow cylinder surface with similar volume, is  $\psi = 0.39$ .

As the microrobot contacts the surface, the surface friction force  $F_f = \mu_f (P - F_b)$ , where  $\mu_f$  is the friction coefficient,  $P$  is the gravitational force, and  $F_b$  is the buoyancy force, will completely dominate the drag force and resist the motion of the microrobot. To reduce the effect of the friction force and effectively control the microrobot along a desired direction ( $\vec{n}$ ), the magnetic force needs to be applied in both  $\vec{n}$  and  $\vec{z}$  directions (i.e., the gravitational direction and the direction perpendicular to  $\vec{n}$ ). The magnetic force acting on the microrobot is defined as:

$$F_m = (\mathbf{m} \cdot \nabla) B \quad (6)$$

where  $\mathbf{m}$  is the magnetic moment of the microrobot. The magnetic force can be divided into two terms that satisfy the following conditions to manipulate the robot (see Figure S9, Supporting Information, for additional details):

$$\begin{cases} F_{m,\vec{n}} \geq F_d \\ F_{m,\vec{z}} \geq P - F_b \end{cases} \quad (7)$$

The translational motion dynamics of the microrobot can be modeled as

$$F_m + F_d + P + F_b = m \frac{dv}{dt} \quad (8)$$

Herein, the magnitude of the magnetic force is directly related to the translational velocity. By changing the magnetic field gradient, the moving velocity of the microrobot can be controlled. From Equation (6), the translational velocity of the microrobot in an equivalent condition ( $\sum F = 0$ ) can be described as:

$$v = \sqrt{\frac{2(\mathbf{m} \cdot \nabla B) \cos \theta}{\rho C_d A}} \quad (9)$$

where  $\theta$  is the angle between the magnetic resultant force and the magnetic force in the  $\vec{n}$  direction:

$$\theta = a \tan \left( \frac{F_{m,\vec{z}}}{\sqrt{F_m^2 + F_{m,\vec{z}}^2}} \right) \quad (10)$$

Through the control of the magnetic fields generated by the eight coils, the microrobot can be stably manipulated. Through the generated magnetic field of the EMA system, the microrobot could be moved in the desired direction and positioned in the working chamber. In brief, the microrobot is controlled with a closed-loop control scheme according to the intensity and direction of the magnetic field gradient as calculated by the PID controller. A microscope (f170, Carl Zeiss) was integrated with the EMA system to observe and record microrobot locomotion. A light source was also placed beside the EMA system to enhance the images of the microrobot locomotion. For the (closed-loop) autonomous control, LifeCam Studio (Microsoft) as a computer vision tracker was used to control the position of the microrobot. The locomotion trajectory was determined by specifying the position (green and blue lines in Figure 4e), and then the position closed-loop control was handled by the PID controller with a tracked position from the camera placed on top of the workspace.

The external uniform magnetic field had an intensity of 40 mT, and the gradient field ranged from 0 to 1.2 T m<sup>-1</sup>. These were applied to move the microrobots along the designed trajectory. The HPV-mimicked fluidic channel was prepared by using a 3D printer (Objet 30 Pro, Staratsys) and coated with 0.5 wt% gelatin for cell culturing and attached to a glass slide using O<sub>2</sub> plasma.

**NIR Triggered Drug Release Test:** For NIR laser irradiation, a continuous-wave fiber-coupled diode laser (with a center wavelength of 808 nm) with external adjustable power (CNI, New Industries Optoelectronics Tech) was used. The power and intensity of the NIR laser were measured by an optical power meter (PM200, Thorlabs). A microrobot was placed in cuvette tubes and the NIR laser irradiated the sample. The distance between the sample and NIR laser was set to 5 cm and the light power was adjusted to 5 W cm<sup>-2</sup>. The time-dependent temperature profile during NIR laser irradiation was obtained using a thermal camera (E60, FLIR), which has a thermal sensitivity of 0.05 °C.

To evaluate the drug-loading properties, the concentration of the remaining DOX solution was measured by a fluorescence spectrophotometer (RF-5301PC, Shimadzu) with excitation at 480 nm. The drug-loading efficiency was calculated as follows: (fluorescence intensity of the feed DOX – fluorescence intensity of DOX in solution)/(fluorescence intensity of feed DOX) × 100%. The drug-releasing test was performed using the microrobot in 1.0 mL of buffer solution (pH = 5.0, 6.0, and 7.4) at 37 °C. The drug concentration in the withdrawn solution was analyzed by measuring the fluorescence intensity. These drug release profiles were evaluated at least three times and cumulative drug release percentages as a function of time were recorded.

**In Vitro Drug Release and Cytotoxicity Test:** Human liver cells (Hep3B) were adopted to verify the proliferation and viability of Hep3B cultured with microrobots. The cells were cultured in a 12-well plate with 2.5 × 10<sup>5</sup> viable cells per well in Dulbecco's Modified Eagle Medium with 10% fetal bovine serum and 1% antibiotic. The cells were cultured for 24 h at 37 °C in a 5% CO<sub>2</sub> constant-temperature, humidified incubator. In the meantime, the microrobots were immersed in 70% alcohol for 10 min to remove the unpolymerized solution while achieving an enhancement in sterilization and washing performance. Afterward, the microrobots were washed with PBS twice to remove the residual alcohol, then autonomously navigated to the target chamber (denoted as *T* in Figure 5a). For the DOX-loaded microrobot, 10 μg of DOX molecules was loaded into each microrobot. Quantification of loaded DOX molecules was optically measured ( $C_{DOX} = (I_{\text{Before}} - I_{\text{After}})/N_{\text{Robot}}$ ). After NIR laser (808 nm and 5 W cm<sup>-2</sup>) irradiation for 10 min, the Hep3B-cell-containing membrane was incubated for 2 h, and then a fluorescence microscopy measurement was performed.

For cellular viability measurement, the NIR-laser-irradiated chamber was further incubated for 24 h after removal of the asymmetric microrobot. Thereafter, a 3-(4,5-dimethylthiazol-2-yl)-2,5-diphenyltetrazolium bromide assay was utilized to evaluate cellular viability. The assay results were recorded at 570 nm using a Bio-Rad 680 microplate reader.

**Statistics and Data Analysis:** Comparisons of all experimental data were analyzed using Student's *t* test. All data were presented as the mean ± SD. The differences between groups of \**P* < 0.05 were considered as statistically significant, and \*\**P* < 0.01 and \*\*\**P* < 0.001 were considered as highly significant.

## Supporting Information

Supporting Information is available from the Wiley Online Library or from the author.

## Acknowledgements

K.T.N. and G.G. contributed equally to this work. The authors thank the Medical Microrobot Center at Chonnam National University for providing facilities and Prof. Kyu-Pyo Kim and Dr. Seonmin Lee, Department of Oncology, Asan Medical Center, University of Ulsan College of Medicine, for supporting the materials. This research was supported by a grant from the Korea Health Technology R&D Project through the Korea Health Industry Development Institute (KHIDI), funded by the Ministry of Health and Welfare, Republic of Korea (Grant No. HI19CO642). This work was also supported by the Korea Medical Device Development Fund grant funded by the Korea government (the Ministry of Science and ICT, the Ministry of Trade, Industry and Energy, the Ministry of Health & Welfare, the Ministry

of Food and Drug Safety) (Project Numbers: 202012D19 and 202012D20), and the National Research Foundation of Korea (NRF) grant funded by the Korea government (MSIT) (No. 2020R1A5A8018367).

## Conflict of Interest

The authors declare no conflict of interest.

## Data Availability Statement

Research data are not shared.

## Keywords

drug delivery, magnetic field control, microrobots, real-time X-ray imaging, shape morphing

Received: September 22, 2020

Revised: December 22, 2020

Published online: January 27, 2021

- [1] N. Bertrand, J. Wu, X. Xu, N. Kamaly, O. C. Farokhzad, *Adv. Drug Delivery Rev.* **2014**, *66*, 2.
- [2] D. Peer, J. M. Karp, S. Hong, O. C. Farokhzad, R. Margalit, R. Langer, *Nat. Nanotechnol.* **2007**, *2*, 751.
- [3] C. D. Walkey, W. C. W. Chan, *Chem. Soc. Rev.* **2012**, *41*, 2780.
- [4] T. M. Allen, P. R. Cullis, *Science* **2004**, *303*, 1818.
- [5] P. Erkoc, I. C. Yasa, H. Ceylan, O. Yasa, Y. Alapan, M. Sitti, *Adv. Ther.* **2019**, *2*, 1800064.
- [6] M. Sitti, H. Ceylan, W. Hu, J. Giltinan, M. Turan, S. Yim, E. Diller, *Proc. IEEE* **2015**, *103*, 205.
- [7] J. Li, T. Li, T. Xu, M. Kiristi, W. Liu, Z. Wu, J. Wang, *Nano Lett.* **2015**, *15*, 4814.
- [8] V. D. Nguyen, J.-W. Han, Y. J. Choi, S. Cho, S. Zheng, S. Y. Ko, J.-O. Park, S. Park, *Sens. Actuators, B* **2016**, *224*, 217.
- [9] Z. Wu, T. Li, W. Gao, T. Xu, B. Jurado-Sánchez, J. Li, W. Gao, Q. He, L. Zhang, J. Wang, *Adv. Funct. Mater.* **2015**, *25*, 3881.
- [10] L. Shao, Z.-J. Yang, D. Andrés, P. Johansson, M. Käll, *ACS Nano* **2015**, *9*, 12542.
- [11] B. Wang, K. F. Chan, J. Yu, Q. Wang, L. Yang, P. W. Y. Chiu, L. Zhang, *Adv. Funct. Mater.* **2018**, *28*, 1705701.
- [12] S. Campuzano, J. Orozco, D. Kagan, M. Guix, W. Gao, S. Satayamasithatit, J. C. Claussen, A. Merkoçi, J. Wang, *Nano Lett.* **2012**, *12*, 396.
- [13] M. Mahmoudi, N. Bertrand, H. Zope, O. C. Farokhzad, *Nano Today* **2016**, *11*, 817.
- [14] H. Hatakeyama, H. Akita, H. Harashima, *Adv. Drug Delivery Rev.* **2011**, *63*, 152.
- [15] X. Wang, X.-H. Qin, C. Hu, A. Terzopoulou, X.-Z. Chen, T.-Y. Huang, K. Maniura-Weber, S. Pané, B. J. Nelson, *Adv. Funct. Mater.* **2018**, *28*, 1804107.
- [16] I. C. Yasa, A. F. Tabak, O. Yasa, H. Ceylan, M. Sitti, *Adv. Funct. Mater.* **2019**, *29*, 1808992.
- [17] Xu H., Medina-Sánchez M., Schmidt O. G., *Angewandte Chemie International Edition* **2020**, *59*, 15029.
- [18] H. Ceylan, I. C. Yasa, O. Yasa, A. F. Tabak, J. Giltinan, M. Sitti, *ACS Nano* **2019**, *13*, 3353.
- [19] U. Bozuyuk, O. Yasa, I. C. Yasa, H. Ceylan, S. Kizilel, M. Sitti, *ACS Nano* **2018**, *12*, 9617.
- [20] G. Go, S.-G. Jeong, A. Yoo, J. Han, B. Kang, S. Kim, K. T. Nguyen, Z. Jin, C.-S. Kim, Y. R. Seo, J. Y. Kang, J. Y. Na, E. K. Song, Y. Jeong, J. K. Seon, J.-O. Park, E. Choi, *Sci. Rob.* **2020**, *5*, eaay6626.
- [21] X. Yan, Q. Zhou, M. Vincent, Y. Deng, J. Yu, J. Xu, T. Xu, T. Tang, L. Bian, Y.-X. J. Wang, K. Kostarelos, L. Zhang, *Sci. Rob.* **2017**, *2*, eaq1155.
- [22] N. Singh, G. J. S. Jenkins, R. Asadi, S. H. Doak, *Nano Rev.* **2010**, *1*, 5358.
- [23] M. Mahmoudi, S. Sant, B. Wang, S. Laurent, T. Sen, *Adv. Drug Delivery Rev.* **2011**, *63*, 24.
- [24] S. Fusco, H.-W. Huang, K. E. Peyer, C. Peters, M. Häberli, A. Ulbers, A. Spyrogiani, E. Pellicer, J. Sort, S. E. Pratsinis, *ACS Appl. Mater. Interfaces* **2015**, *7*, 6803.
- [25] H.-W. Huang, M. W. Tibbitt, T.-Y. Huang, B. J. Nelson, *Soft Rob.* **2019**, *6*, 150.
- [26] J. C. Breger, C. Yoon, R. Xiao, H. R. Kwag, M. O. Wang, J. P. Fisher, T. D. Nguyen, D. H. Gracias, *ACS Appl. Mater. Interfaces* **2015**, *7*, 3398.
- [27] K. Malachowski, J. Breger, H. R. Kwag, M. O. Wang, J. P. Fisher, F. M. Selaru, D. H. Gracias, *Angew. Chem., Int. Ed.* **2014**, *53*, 8045.
- [28] A. Ghosh, Y. Liu, D. Artemov, D. H. Gracias, *Adv. Healthcare Mater.* **2020**, 2000869.
- [29] S. Jeon, S. Kim, S. Ha, S. Lee, E. Kim, S. Y. Kim, S. H. Park, J. H. Jeon, S. W. Kim, C. Moon, *Sci. Rob.* **2019**, *4*, eaav4317.
- [30] J. Li, X. Li, T. Luo, R. Wang, C. Liu, S. Chen, D. Li, J. Yue, S.-h. Cheng, D. Sun, *Sci. Rob.* **2018**, *3*, eaat8829.
- [31] T. Wei, J. Liu, D. Li, S. Chen, Y. Zhang, J. Li, L. Fan, Z. Guan, C. M. Lo, L. Wang, *Small* **2020**, *16*, 1906908.
- [32] G. Go, S.-G. Jeong, A. Yoo, J. Han, B. Kang, S. Kim, K. T. Nguyen, Z. Jin, C.-S. Kim, Y. R. Seo, *Sci. Rob.* **2020**, *5*, eaay6626.
- [33] J. Park, J. Y. Kim, S. Pané, B. J. Nelson, H. Choi, *Adv. Healthcare Mater.* **2020**, 2001096.
- [34] D. I. Kim, H. Lee, S. H. Kwon, Y. J. Sung, W. K. Song, S. Park, *Adv. Healthcare Mater.* **2020**, *9*, 2000118.
- [35] O. Felfoul, M. Mohammadi, S. Taherkhani, D. de Lanauze, Y. Z. Xu, D. Loghini, S. Essa, S. Jancik, D. Houle, M. Lafleur, L. Gaboury, M. Tabrizian, N. Kaou, M. Atkin, T. Vuong, G. Batist, N. Beauchemin, D. Radzioch, S. Martel, *Nat. Nanotechnol.* **2016**, *11*, 941.
- [36] F. Ullrich, C. Bergeles, J. Pokki, O. Ergeneman, S. Erni, G. Chatzipirpiridis, S. Pané, C. Framme, B. J. Nelson, *Invest. Ophthalmol. Visual Sci.* **2013**, *54*, 2853.
- [37] J. Li, B. Esteban-Fernández de Ávila, W. Gao, L. Zhang, J. Wang, *Sci. Rob.* **2017**, *2*, eaam6431.
- [38] B. J. Nelson, I. K. Kaliakatsos, J. J. Abbott, *Annu. Rev. Biomed. Eng.* **2010**, *12*, 55.
- [39] E. S. Olson, J. Orozco, Z. Wu, C. D. Malone, B. Yi, W. Gao, M. Eghtedari, J. Wang, R. F. Mattrey, *Biomaterials* **2013**, *34*, 8918.
- [40] D. Vilela, U. Cossío, J. Parmar, A. M. Martínez-Villacorta, V. Gómez-Vallejo, J. Llop, S. Sánchez, *ACS Nano* **2018**, *12*, 1220.
- [41] Z. Xu, M. Chen, H. Lee, S.-P. Feng, J. Y. Park, S. Lee, J. T. Kim, *ACS Appl. Mater. Interfaces* **2019**, *11*, 15727.
- [42] S. Jeon, S. Kim, S. Ha, S. Lee, E. Kim, S. Y. Kim, S. H. Park, J. H. Jeon, S. W. Kim, C. Moon, B. J. Nelson, J.-y. Kim, S.-W. Yu, H. Choi, *Sci. Rob.* **2019**, *4*, eaav4317.
- [43] H.-W. Huang, M. W. Tibbitt, T.-Y. Huang, B. J. Nelson, *Soft Rob.* **2018**, *6*, 150.
- [44] J. Li, X. Li, T. Luo, R. Wang, C. Liu, S. Chen, D. Li, J. Yue, S.-h. Cheng, D. Sun, *Sci. Rob.* **2018**, *3*, eaat8829.
- [45] D.-i. Kim, H. Lee, S.-h. Kwon, H. Choi, S. Park, *Sens. Actuators, B* **2019**, *289*, 65.
- [46] V. Iacovacci, L. Ricotti, E. Sinibaldi, G. Signore, F. Vistoli, A. Menciassi, *Adv. Sci.* **2018**, *5*, 1800807.
- [47] M. Revilla-León, M. J. Meyers, A. Zandinejad, M. Özcan, *J. Esthetic Restor. Dent.* **2019**, *31*, 51.
- [48] J. H. Ryu, P. B. Messersmith, H. Lee, *ACS Appl. Mater. Interfaces* **2018**, *10*, 7523.

- [49] G. Go, J. Han, J. Zhen, S. Zheng, A. Yoo, M. J. Jeon, J. O. Park, S. Park, *Adv. Healthcare Mater.* **2017**, *6*, 1601378.
- [50] Z. Jin, K. T. Nguyen, G. Go, B. Kang, H. K. Min, S. J. Kim, Y. Kim, H. Li, C. S. Kim, S. Lee, S. Park, K. P. Kim, K. M. Huh, J. Song, J. O. Park, E. Choi, *Nano Lett.* **2019**, *19*, 8550.
- [51] D. Bang, T. Lee, J. Choi, Y. Park, E. Kim, Y. M. Huh, S. Haam, *Adv. Healthcare Mater.* **2014**, <https://doi.org/10.1002/adhm.201400197>.
- [52] S. Shen, S. Wang, R. Zheng, X. Zhu, X. Jiang, D. Fu, W. Yang, *Biomaterials* **2015**, *39*, 67.
- [53] J. Estelrich, M. A. Busquets, *Molecules* **2018**, *23*, 1567.
- [54] V. D. Nguyen, H. K. Min, D. H. Kim, C. S. Kim, J. Han, J. O. Park, E. Choi, *ACS Appl. Mater. Interfaces* **2020**, <https://doi.org/10.1021/acami.9b23632>.
- [55] C. R. Justus, L. Dong, L. V. Yang, *Front Physiol.* **2013**, *4*, 354.
- [56] J. H. Son, B. Cho, S. Hong, S. H. Lee, O. Hoxha, A. J. Haack, L. P. Lee, *Light: Sci. Appl.* **2015**, *4*, e280.
- [57] J. Han, J. Zhen, V. Du Nguyen, G. Go, Y. Choi, S. Y. Ko, J. O. Park, S. Park, *Sci. Rep.* **2016**, *6*, 28717.
- [58] B. S. Zolnik, D. J. Burgess, *J Control Release* **2007**, *122*, 338.
- [59] H. Yu, Z. Cui, P. Yu, C. Guo, B. Feng, T. Jiang, S. Wang, Q. Yin, D. Zhong, X. Yang, *Adv. Funct. Mater.* **2015**, *25*, 2489.
- [60] C. Wang, H. Xu, C. Liang, Y. Liu, Z. Li, G. Yang, L. Cheng, Y. Li, Z. Liu, *ACS Nano* **2013**, *7*, 6782.
- [61] E. Ahnfelt, O. Degerstedt, E. Lilienberg, E. Sjögren, P. Hansson, H. Lennernäs, *J. Drug Delivery Sci. Technol.* **2019**, *53*, 101143.
- [62] J.-M. Idée, B. Guiu, *Crit. Rev. Oncol./Hematol.* **2013**, *88*, 530.
- [63] A. Pena-Francesch, J. Giltinan, M. Sitti, *Nat. Commun.* **2019**, *10*, 3188.
- [64] W.-H. Zhou, C.-H. Lu, X.-C. Guo, F.-R. Chen, H.-H. Yang, X.-R. Wang, *J. Mater. Chem.* **2010**, *20*, 880.
- [65] K. E. Peyer, L. Zhang, B. J. Nelson, *Nanoscale* **2013**, *5*, 1259.
- [66] M. Hartman, O. Trnka, K. Svoboda, *Ind. Eng. Chem. Res.* **1994**, *33*, 1979.
- [67] R. P. Chhabra, L. Agarwal, N. K. Sinha, *Powder Technol.* **1999**, *101*, 288.